TITLE:

Solar-Driven Electrochemical Green Fuel Production from CO_2 and Water Using $Ti_3C_2T_x$ MXene-Supported CuZn and NiCo Catalysts

AUTHORS AND AFFILIATIONS:

Nusrat Rashid[1]*, Shurui Yang[1], Preetam Kumar Sharma[1], Zahra Albu[1], Anupma Thakur[2], Babak Anasori[2,3], Mojtaba Abdi-Jalebi[1]*

[1]Institute for Materials Discovery, University College London, Malet Place, London WC1E 7JE, UK
[2]School of Materials Engineering, Purdue University, West Lafayette, IN 47907, United States
[3]School of Mechanical Engineering, Purdue University, West Lafayette, IN 47907, United States

Email addresses of the co-authors:
Shurui Yang shurui.yang.22@ucl.ac.uk
Preetam Kumar Sharma preetam.sharma@ucl.ac.uk
Zahra Albua zahra.albu.22@ucl.ac.uk
Anupma Thakur thakur40@purdue.edu
Babak Anasori banasori@purdue.edu

*Email address of the corresponding authors:
Nusrat Rashida (nusrat.rashid@ucl.ac.uk)
Mojtaba Abdi-Jalebia (m.jalebi@ucl.ac.uk)

SUMMARY:

This protocol guides the fabrication and electrochemical analysis of MXene-supported CuZn and NiCo bi-metallic electrocatalysts for green fuel production from carbon dioxide and water using solar energy.

ABSTRACT:

This protocol describes the synthesis and activity mapping of bi-metallic, MXene-supported cathodes for carbon dioxide reduction (CO_2R) and anodes for water splitting utilizing solar energy in alkaline media. A reverse current pulse electrodeposition technique was used to control the nanostructure, grain refinement, and alloy composition of the fabricated electrodes. Both anodes and cathodes are noble metal-free and supported on two-dimensional (2D) titanium carbide ($Ti_3C_2T_x$) MXene, which reduces contact resistance and facilitates the charge transfer from substrate to reactants via catalysts. Copper zinc (CuZn) supported on $Ti_3C_2T_x$ MXene are used as cathodes for methanol production in thermocatalytic CO_2 conversion, and here we have demonstrated their performance in electrochemical CO_2 reduction (CO_2R) for the first time. Nickel cobalt (NiCo) supported on $Ti_3C_2T_x$ MXene are similarly fabricated via pulse electrodeposition and tested as anodes for water electrolysis driven by a solar cell under simplified laboratory conditions. The activity also describes the structural characterization of metallic thin films. Detailed set-up of PV integration with electrochemical cell which in-turn feeds in-line gas chromatography is demonstrated for both CO_2R and water electrolysis (WE). A set-up detailing the water electrolysis at commercial conditions of highly caustic alkaline solutions (30

% KOH), high temperatures (60 °C), and in zero-gap cell is demonstrated on the fabricated anode paired with Pt/C spray coated cathode.

INTRODUCTION:

Replacing fossil fuels with zero-emission alternatives is critical to decarbonizing the energy sector and increasing the use of renewable energy[1–3]. Conversion of carbon dioxide (CO_2) into carbon monoxide (CO), methane (CH_4), and other carbonaceous fuels is becoming an important route to prevent further CO_2 emissions and create a circular carbon economy [4] . Similarly, replacing fossil fuels with high energy density hydrogen is projected to accelerate the energy transition from fossil-based to zero-emission fuels[5–8] The energy generation system can be further made cost-effective, and eco-friendly by using direct sunlight[9–12]. The green energy transition can generate positive socio-economic outcomes, particularly by enhancing social impacts and thereby increasing the social capital associated with zero-emission fuel generation[13].

An extensive body of research has been dedicated towards solar-driven electrochemical reduction of CO_2 and hydrogen generation[14,15]. Copper based materials have shown excellent activity (>70% faradaic efficiency towards C_2 product) towards CO_2 reduction[16–19]. Bimetallic systems consisting of copper leads to increase in Faradaic Efficiencies (FE) and overall carbon dioxide conversion rate. The main challenges are high overpotentials, lower faradaic efficiencies and selectivity of a single product[20]. Integrating photovoltaic (PV) systems with electrochemical reactions requires an overlap between the electrocatalyst's faradaic activity and the solar cell's maximum power point to achieve sustainable fuel production rates[21]. Ni and Co bimetallic systems have been extensively reported as high functional anodes for alkaline water electrolysis due to their < 600 mV overpotential at currents > 100 mA/cm^2 [22,23]. Rapid degradation of catalyst at industrially relevant currents limits their viability as commercial anodes. The electrolyte induced short circuiting by corrosion of interface between metal layer and substrate further makes water electrolysis sluggish[24,25].

MXenes, a growing family of two-dimensional (2D) transition metal carbides, nitrides, and carbonitrides, have emerged as promising materials for electrochemical CO_2R reaction due to their unique structural and electronic properties[26,27]. First discovered in 2011, MXenes are mostly derived from bulk-layered $M_{n+1}AX_n$ phases (where n = 1- 4) which consists of n+1 layers of one or more transition metals (M, typically from groups 4-6), interleaved with X layers, carbon (C), nitrogen (N) or both (CN), and an A group element (usually from groups 13-16). Their compositions can be tuned using different transition metals of groups 4 to 6, X sublattice (C/N), and T_x represents surface terminations (e.g., -O, -OH, -F, -Cl)[26,28,29]. In CO_2R, MXenes are being actively investigated as co-catalysts or supports due to their tunable surface chemistry, catalytically active sites, high specific surface area, and metal-like electrical conductivity.

Recent theoretical studies predict that decorating MXenes with bimetallic or single atoms can substantially enhance CO_2R performance by modulating their electronic structure. These design strategies shift the d-band center, modulate the intermediate adsorption energies, and lowers the Gibbs free energy barriers of rate-determining steps[30–32]. For instance, Mo_2ZC_2 MXenes (Z = Ti, V, etc.) have been shown to strengthen $-HOCH_2O$ adsorption and weaken $-OCH_2O$ binding in electrochemical CO_2RR, thereby reducing the limiting potential for CH_4 production due to an upshift in the d-band center of Mo atoms. In another study, Cu-doped $Ti_3C_2T_x$ MXene achieved a Faradaic efficiency of 58.1% toward $HCOO^-$ production by introducing polarized sites that facilitate intermediate adsorption and electron transfer. These few theoretical studies guide the potential of exploring MXene-based bimetallic catalysts in tailoring CO_2RR pathways.

Here, we have synthesized CuZn@$Ti_3C_2T_x$ MXene cathodes and NiCo@$Ti_3C_2T_x$ MXene anodes for CO_2R and water electrolysis by simple one pot electrodeposition. The optimized procedure can be used to deposit a range of bi-metallic or polymetallic systems in concentration ranges from 5 to 100mM each with pH control. Each set of desired system would demand to tune the pH and current density according to their electrochemical potentials, deposition potential, reaction conditions, etc. Although, the deposition can be carried on a two-electrode setup, better control over the deposition voltage through reference electrodes is advised. The method can deposit large structures as well as fine particles with controlling reaction parameters like current density, ON-OFF time ratio, and pH. The refined and optimized grain structure tuned by reverse current pulses shows high Faradaic efficiency (56% for hydrocarbons) for CO_2R with very low catalyst degradation. Water electrolysis is demonstrated on NiCo@$Ti_3C_2T_x$ MXene in H-cell for laboratory conditions with 98% FE and in zero-gap cell for industrial conditions. A demonstration of in-line product determination by gas chromatography is also featured. The overall system integration and its operation have been closely monitored using the safe by design protocols established in our lab[33].

PROTOCOL:

1 Synthesis of $Ti_3C_2T_x$ MXene

1.1 Wash 1 g of optimized Ti_3AlC_2 MAX phase using 9 M hydrochloric acid (HCl) for 18 hours to remove intermetallic impurities.

1.2 Prepare the etchant solution by mixing 12 M HCl, deionized (DI) water, and 50 wt% hydrofluoric acid (HF) in a 6:3:1 volume ratio.

Notes: Hydrofluoric acid (HF) is highly toxic and corrosive. Perform all steps involving HF in a certified fume hood while wearing appropriate personal protective equipment (PPE), including gloves, lab coat, and face shield.

1.3 Add the HCl-washed MAX powder to the etchant solution and stir at 400 RPM for 24 hours at 35 °C.

1.4 Wash the etched $Ti_3C_2T_x$ MXene with DI water by repeated centrifugation at 3234 RCF for 4–5 cycles (~200 mL each), each cycle of 10 minutes, until the supernatant reaches a neutral pH of approximately 6.

1.5 Delaminate the MXene by adding the washed sediment to a lithium chloride (LiCl) solution (50 mL per gram of etched powder) and stir at 400 RPM for 1 hour at 65 °C under argon gas flow.

1.6 Wash the mixture by centrifugation at 3234 RCF for 5, 10, 15, and 20 minutes sequentially at room temperature.

1.7 Vortex mix the final suspension for 30 minutes at room temperature, then centrifuge at 2380 RCF for 30 minutes to obtain single-to-few-layered $Ti_3C_2T_x$ MXene flakes.

2 Preparation of Precursors

2.1 Disperse 300 mg of $Ti_3C_2T_x$ MXene in 100 mL of DI water. Sonicate for 5 minutes to ensure stable dispersion.

2.2 Prepare a 30 mM copper citrate solution and a 10 mM zinc oxalate solution in DI water. Ensure to make all solutions in a hood with proper PPE avoiding spillage or direct contact with skin.

2.3 Prepare 50 mM solutions of nickel nitrate and cobalt nitrate in DI water.

2.4 Prepare a dispersion of 5 mg of Pt/C in 50 mL of DI water and sonicate for 10 minutes at room temperature.

3 Fabrication of Electrodes

3.1 Clean the nickel foam using acetone and then sonicate in DI water for 5 minutes.

3.2 Activate the carbon fiber paper (CFP) by soaking in 1 M nitric acid (HNO_3) for 20 minutes. Activate the CFP in a hood and use gloves and proper PPE.

3.3 Immerse the cleaned nickel foam (5 cm × 5 cm) in MXene solution for 5 minutes. Dry at room temperature under vacuum. Label this sample as MXene-Ni-Foam.

3.4 Spray-coat MXene solution onto activated CFP. Label the sample as MXene-CFP. Load 50 mL of Mxene solution in a spray gun. At a distance of 5 cm spray the ink on activated CFP covering whole surface of 2 cm *2 cm CFP.

3.5 In a glass electrochemical cell, add the Cu and Zn precursor solutions. Use an Ag/AgCl reference electrode, a platinum counter electrode, and MXene-CFP as the working electrode and connect the electrodes to respective connection on the potentiostat. For example, Mxene-CFP electrode will be connected to working electrode connection and likewise. The electrolyte bath consisted of 50 mL of 30 mM Cu citrate solution and 10 mM of Zn oxalate in DI water.

3.6 Apply the following pulsed current deposition sequence:

- -10 mA/cm^2 for 1 s,
- 0 mA/cm^2 (null pulse) for 0.5 s,
- +10 mA/cm^2 for 0.5 s.

3.7 Repeat for 1000 cycles to deposit CuZn. Label the resulting electrode as CuZn@$Ti_3C_2T_x$-MXene-CFP.

3.8 In another cell, add Ni and Co precursor solutions. Use the same electrode configuration but replace the working electrode with MXene-Ni-Foam. Ensure the electrodes in the electrochemical cell are connected properly with respective connections on potentiostat. The electrolytic bath consists of 50 mL of 50 mM of Ni nitrate and Co nitrate in DI water.

3.9 Apply the same pulsed deposition cycle (as in 3.6) for 1000 sets to obtain NiCo@$Ti_3C_2T_x$-MXene-Ni-Foam.

3.10 Fill 50 mL of Pt/C in spray gun. From a distance of 5 cm, spray-coat Pt/C onto Ni mesh and dry in vacuum oven at 60 °C to prepare the reference cathode for water electrolysis.

4 Structural Characterization

4.1 Cut each electrode into 0.5 × 1 cm pieces.

4.2 Perform X-ray diffraction (XRD) and scanning electron microscopy (SEM) for phase and morphology analysis.

Notes: The size of electrode pieces should be similar to what fits to XRD and SEM instrument sample preparation guidelines.

5 Electrochemical CO_2 Reduction

5.1 Assemble an H-cell with an alkaline exchange membrane separating the two chambers.

5.2 Use Ni-Foam as anode and CuZn@$Ti_3C_2T_x$-MXene-CFP (2 cm × 2 cm) as cathode. Use 1 M KOH as an electrolyte in both chambers. Check thoroughly for any electrolyte leaks at membrane junction. Tighten the junction for any leak.

Notes: KOH is highly corrosive, wear proper PPE and make all solutions in a fume hood and avoid contact with skin. Keep all solutions on flat surfaces away from personal intrusion and electrical plugs.

5.3 Insert a Hg/HgO reference electrode in the cathode compartment. Seal the system to be gas tight. Add a tubing for CO_2 inlet and one for gas outlet in cathodic chamber.

5.4 Purge CO_2 into the cathodic chamber at 30 mL/min for 15 minutes to saturate the electrolyte.

5.5 Illuminate the photovoltaic (PV) cell with 1-sun intensity and connect it to the cell (positive to anode, negative to cathode).

5.6 Record cyclic voltammetry (CV) from 0 V to -2.5 V at 50 mV/s and EIS (100 kHz to 0.1 Hz) at open circuit potential.

5.7 Perform a 0 A chrono potentiometric measurement for 2 hours, recording current periodically using a multimeter. The recorded current can be used to calculate faradaic efficiency of products.

5.8 Connect the cathodic chamber outlet to a gas chromatograph (GC) for in-line sampling every 10 minutes. Program the GC for detection and quantification of permanent gases. Use a packed column like Molecular sieve to identify the gases. The temperature of oven is set at ramping with initial temperature of 150 ^oC with a hold time of 2 minutes and further ramped to 200 ^oC with a hold time of 1 minute to allow proper separation and elution of the gases from mixture.

6 Electrochemical Water Electrolysis (OER)

6.1 Repeat the H-cell setup with NiCo@$Ti_3C_2T_x$-MXene-Ni-Foam as anode and Pt/C@Ni mesh as cathode. Insert an Hg/HgO electrode as reference electrode in anodic chamber with the working electrode.

6.2 Fill both chambers with 1 M KOH electrolyte.

6.3 Record CV from 0 V to 1.2 V at 50 mV/s and EIS (10 kHz to 0.1 Hz, 10 mV amplitude) at open circuit potential. On autolab potentiostat use OCP (open circuit potential) determination function to record OCP.

6.4 Illuminate the PV cell with 1-sun light using a solar simulator placed 5 cm away.

6.5 Connect PV terminals to electrodes and record a 0 A chrono potentiometric curve. Monitor and log current for efficiency calculations.

6.6 Connect the cathode outlet to GC and analyze hydrogen production every 10 minutes using a thermal conductivity detector (TCD) with nitrogen as carrier gas.

7 Zero-Gap Electrolyzer Assembly

7.1 Wash with water and prepare a zero-gap cell. Prepare clean polyvinyl propylene tubing and other accessories like push and pull values that fit to the tubing to create junctions between various parts of alkaline water electrolysis assembly.

7.2 Stack the following in sequence: Cell anode plate, NiCo@$Ti_3C_2T_x$-MXene-Ni-Foam anode, gasket (same or slightly thicker (0.1 mm) than the thickness of anode), alkaline exchange membrane, gasket, Pt/C cathode, and finally cathode cell plate. Use positioning rods for alignment if available or make sure to keep the layers firm and stationary on a table.

7.3 Assemble the electrolyzer with proper alignment of all layers and end plates. Secure tightly using screws.

7.4 Connect the cell to peristaltic pumps circulating 30 % KOH at 30 mL/min. The flow rate of electrolyte can be adjusted and depending on the gas evolution and temperature of electrolyte can be increased for better gas removal and activity.

7.5 Maintain the electrolyte reservoir at 60 °C using an oil bath and monitor with a temperature probe. Ensure not touching the cell or reservoir without thermal gloves.

Notes: 30 % KOH is highly caustic and can cause burns. Perform all experiments in proper personal protective equipment. Store extra electrolyte in fume hood and keep electrolyte reservoir on flat surface and well supported and balanced to avoid spills.

8 Calculation of Faradaic Efficiency

8.1 Use the following equation:

$$FE(\%) = \frac{Q_{prod}}{Q_{total}} \times 100\%$$

Where Q_{prod} is the charge used to form the product (e.g., hydrogen or CO_2R product), and Q_{total} is the total charge passed.

Note: Dispose of all HF- and HCl-containing waste following institutional hazardous waste protocols. Consult Material Safety Data Sheets (MSDS) and environmental health and safety (EHS) personnel for disposal guidance.

REPRESENTATIVE RESULTS:

X-ray diffraction technique is used to analyse the solid crystal structure of the metal films. Cut appropriately sized (fits to the sample stub of XRD machine) film samples. Load the samples in the machine and scan range of $2\ \Theta$ from $10\ ^{o}$ to $80\ ^{o}$. The XRD graph obtained shows peak signals for the crystal planes present in the material. Use ICDD reference pattern to identify and further analyse the crystal structure like main peaks, d-spacing, peak shifts due to alloy formation. Scanning electron microscopy (SEM) is used to show the microscopic structure and topology of the deposited material. SEM images show the shape, size, and conformality of the film.

X-ray diffraction (XRD) pattern and scanning electron microscope (SEM) images obtained for Ti_3AlC_2 MAX phase, and $Ti_3C_2T_x$ MXene are shown in **Figure 1**. The diffraction pattern of Ti_3AlC_2 MAX exhibited characteristic (002) peaks for M_3AlC_2 structure, and after the selective etching and delamination, the (002) peaks shift to lower angles suggesting the synthesis of $Ti_3C_2T_x$ MXene (**Figure 1A**). SEM image of the Ti_3AlC_2 MAX phase reveal its layered morphology (**Figure 1 B**). After selective etching of Ti_3AlC_2 MAX and delamination of multilayered $Ti_3C_2T_x$ MXene, the delaminated $Ti_3C_2T_x$ MXene deposited on an alumina anodic exhibit a flake-like morphology consisting of single to few-layers as shown in the SEM image (**Figure 1C**).

XRD and Scanning electron microscopic images of CuZn@$Ti_3C_2T_x$ MXene@CFP and NiCo@$Ti_3C_2T_x$ MXene@Ni-Foam are shown in **Figure 2A-B**. **Figure 3** shows the PV cell, H-cell, solar driven gas evolution, and zero-gap cell assembly with electrolyte flow. **Figure 4** shows (A) CV in CO_2 reduction and water electrolysis, (B) EIS in H-cell for cathode in CO_2 reduction and anode in water electrolysis, and (C) CV on anode for a full cell. A supplementary information contains supplementary figures S1 showing EIS @OCP in zero-gap cell, S2 shows gas chromatograms on

TCD and FID for CO_2 reduction and S3 shows gas chromatograms for water electrolysis.

FIGURE LEGENDS:

Figure 1: (A) XRD pattern showing characteristic peaks for $Ti_3C_2T_x$ (indicated by stars) and Ti_3AlC_2 MAX phase (indicated by diamonds); (B) SEM image of Ti_3AlC_2 MAX phase; (C) SEM image of delaminated $Ti_3C_2T_x$ MXene.

Figure 2: XRD (A) and SEM images of the fabricated bi-metallic electrocatalyst films, CuZn@$Ti_3C_2T_x$ MXene@CFP cathode for CO_2 reduction (B and C), and NiCo@$Ti_3C_2T_x$ MXene@Ni-F anode for water electrolysis (D and E).

Figure 3: (A) PV assembly used to drive the electrochemical reduction of CO_2 and water at zero applied current, (B) H-cell used to reduce CO_2 and electrolyze water with a membrane to stop product oxidation, (C) gas bubbles observed on cathode when connected to the terminals of PV cell showing the reaction taking place, and (D) zero-gap cell assembly used to perform water electrolysis at industrial parameters (30% KOH, 1 A/cm^2, 60 ^oC).

Figure 4: (A) CV obtained in 1 M KOH in a H-cell for CO_2 reduction (CO_2R) (red trace), and OER (blue trace) using H-cell assembly, (B) EIS at open circuit potential for anode and cathode in CO_2R and water electrolysis, (C) CV and (D) chrono amperograms observed at different applied cell potentials (1.6 V to 2.6 V on NiCo@MXene@Ni-Foam anode in 30% KOH, 60 ^oC, and electrolyte flow rate of 50 mL/min in a zero-gap cell (mimicking commercial AEM-WE).

Figure S1: EIS recorded at 0V on NiCo@MXene@Ni-Foam anodes in a zero-gap cells. The total cell resistance is <1ohm showing high conductivity.

Figure S2: Gas chromatograms at TCD 1, 2 and FID detectors operating at method specially created for detection and identification of permanent gases in CO_2 reduction (a) FID, (b) TCD1, and (c) TCD2. The peaks for CH_4, C_2H_4, C_2H_6, H_2 are detected with comparison to calibration curve computed using standard concentrations for these cases.

Figure S3: Gas chromatograms at TCD 1 and FID detectors operating at method specially created for detection and identification of hydrogen and oxygen (a) TCD, and (b) FID. The peaks for H_2 and O_2 are detected with comparison to calibration curve computed using standard concentrations for these gases. It can be seen we have no signal on FID for water splitting is expected.

DISCUSSION:

Here, we present the protocol for synthesis of bi-metallic electrodes for solar driven redox reaction for fuel generation. Decarbonizing the energy sector heavily depends on CO_2 conversion [34–36] and use of zero-emission fuels like hydrogen generated from water[37,38]. Solar driven electrochemical transformation of carbon dioxide and water needs a combination of catalysts (anodes and cathodes) that function at the peak performance of the PV cell used[10] . H-cell is used to separate anodic and cathodic products and to prevent re-oxidation of cathodic products at the anode. The alkaline exchange membrane should be placed carefully between two halves of the cell that will lead to better transport of ions and avoiding gas crossover.

We show that electrodeposition can be used to deposit metallic catalysts depending on the desired reaction and structure. A pulsed deposition offers more control over the microscopical structure and alloy composition compared to constant deposition[39,40]. On applying a negative pulse, the positively charged metal ions are dragged to cathode where they are discharged and deposited as metal particles. A null pulse repopulates the electron diffusion layer thus controlling the grain size and texture. A reverse pulse refines the grain and optimizes the alloy composition[41–43]. The method used in this activity is combination of forward (-ve amplitude pulse), null (zero amplitude pulse), and reverse (+ve amplitude pulse) repeated 1000 times to deposit a thin conformal catalyst layer shown in **Figure 1.** CuZn@$Ti_3C_2T_x$ MXene@CFP shows nano-sheet structure and a conformal deposition on CFP. NiCo@$Ti_3C_2T_x$ MXene@Ni-Foam shows the compact film deposited on the nickel foam. It is important to optimize the metal ratio in precursor for a desired alloy composition. From XRD graphs (**Figure 2A)**, the phase obtained is α-brass with copper content around 64% and Zn about 36%. [44] The NiCo bi-metallic system is deposited in FCC phase with metallic Ni, Co and Ni-Co alloy with 1:1 ratio [45]. The electrochemical potential of metal ions plays a crucial role in deposition process, thus required attention[46,47].

Electrochemical reduction of CO_2 is done in an H-cell which is gas tight and in-line with GC. To analyze the electrochemical performance a CV at 50 mV/s scan rate is recorded in 1 M KOH in a 3-electrode setup. A 3-electrode setup includes reference electrode which monitors working electrode potential to compare the activity and overpotential to state-of-art materials for CO_2 to fuels. An EIS is used to determine the charge transfer resistance and total IR losses associated with the cell, electrolyte, substrate and catalysts. The PV cell illuminated with 1 sun light is connected with the H-cell and left to run for 2 hours. The gas evolved from the cell is fed to GC to analyze the products formed every 10 minutes. A method that uses thermal conductivity detector and flame ionization detector to detect the CO_2 products is used in loops to identify and quantify the gases generated. A calibration curve generated by using standard concentration of permanent gases (O_2, N_2, CO, CH_4, C_2H_4, C_2H_6 etc) is used to calculate the faradaic efficiency of products obtained in the CO_2R[48,49].

A CV and EIS were recorded in H-cell with NiCo@$Ti_3C_2T_x$ MXene@Ni-Foam as anode, Pt/C as cathode and Hg/HgO as reference electrode and 1M KOH as electrolyte at scan rate of 50 mV/s and open circuit potential respectively to assess the electrochemical activity of the cathode. To test the solar driven water electrolysis performance, illuminated PV cell terminals were connected to H-cell electrodes (anode and cathode) and a chronopotentiometric curve was recorded at zero applied current. The cell was gas tight and connected to GC to quantify the hydrogen produced every 10 minutes. The GC method used TCD in single loops to quantify the hydrogen produced by comparing the peak area and flow rate of gas (H_2, O_2, N_2 (carrier gas)) from cell with calibration curve generated using standard concentration of hydrogen. It is important to take care while measuring the area under the hydrogen peak for consistent results.

A zero-gap cell is used to limit the IR losses prevalent in H-cell. Standard industrial conditions of electrolyte concentration (30 % KOH), current densities (1 A/cm^2), and temperatures (60 ^oC) were used to show hydrogen production at commercial demands. Care must be taken while assembling zero gap cell to avoid any leak of electrolyte or gas. Using screws to keep in place the end plate, place the anode on the flow channel and secure it in place by using a gasket, now layer AEM (moist and activated in 1 M KOH for 24 hours), and secure with a gasket, then add the counter electrode and second end plate and tighten the screws to stop any leaking. Connect the inlet of zero gap cell with outlet of peristaltic pumps and outlet of cell to electrolyte reservoir (30 % KOH) that is held at 60 ^oC. The pump inlet is connected to the electrolyte reservoir. An applied current of 10 kA/m^2 is used to study the performance of the cell and durability of catalysts. Cell voltage observed gives insights into the performance, and degradation/change of cell voltage over time gives insights into durability of the cell system. A good heat exchanger is needed to maintain the desired temperature of the electrolyte flow. Ensuring no leak from cell or any connecting tubing is vital to avoid performance loss and risk mitigation.

The method of deposition has practical application in fabricating thin metal films for catalyst coated substrate electrolysers. The deposition method can be used with small adjustments to coat a surface with poly-metal alloys of choice for other electrocatalytic applications. The water electrolysis in zero-gap cell under industrial conditions can be used to generate hydrogen at higher quantities with scaling up.

Troubleshooting details: It is important to take necessary precautions in terms of safety and execution of the reaction with precisely controlled parameters. However, due to asymmetric personal and instrumental errors, the experiment can fail. Confirm the connections from electrochemical cell and electrodes are well established and not rusty. For PV connection test if on illumination potential/current is generated to draw the reaction. For electrodeposition keep counter and working electrodes facing each other with reference electrode near to working electrode without blocking its front side. The electrodeposition method should work for all first-row transition metals and can be diversified using higher or lower current ON pulses and pH adjustments. Normally only metallic films can be obtained via this method but for oxide films, oxidative potential can be applied. The electrodeposition is limited by the nature of metals and the current amplitude, an unoptimized current amplitude and concentration of metals leads to asymmetrical and coarse deposition that hampers the reaction considerably. The extent of hydrogen generation or CO_2 products is decided by area of electrode, intrinsic activity of electrode, nature of substrate, potential limit of the instrument, and gas transport from electrode to outside.

ACKNOWLEDGMENTS:

The authors wish to acknowledge the support of the Henry Royce Institute for Advanced Materials through the Industrial Collaboration Programme (RICP-R4-100061) and MATceleratZero (MATZ0), funded from a grant provided by the Engineering and Physical Sciences Research Council EP/X527257/1. The authors acknowledge the Department for Energy Security and Net Zero (Project ID: NEXTCCUS), University College London's Research, Innovation and Global Engagement, University of Sydney – University College London Partnership Collaboration Awards, UCL-Peking University Strategic Partner Funds, Cornell-UCL Global Strategic Collaboration Awards and IISc-UCL Joint seed fund for their financial support. The authors acknowledge the ACT program (Accelerating CCS Technologies, Horizon2020 Project No. 691712) for the financial support of the NEXTCCUS project (project ID: 327327). This work was supported by the Henry Royce Institute for advanced materials through the Equipment Access Scheme enabling access to the Royce SEM-FIB Suite at Cambridge; Cambridge Royce facilities grant EP/P024947/1 and Sir Henry Royce Institute – recurrent grant EP/R00661X/1.

DISCLOSURES:

Authors have nothing to disclose.

REFERENCES:

1. Brauns, J. & Turek, T. Alkaline Water Electrolysis Powered by Renewable Energy: A Review. *Processes 2020, Vol. 8, Page 248* **8**, 248 (2020).
2. Dinh, C. T., Li, Y. C. & Sargent, E. H. Boosting the Single-Pass Conversion for Renewable

Chemical Electrosynthesis. *Joule* **3**, 13–15 (2019).

3. Züttel, A. *et al.* Storage of Renewable Energy by Reduction of CO2 with Hydrogen. *Chimia (Aarau)* **69**, 264–8 (2015).
4. Liu, S. *et al.* To convert or not to convert: A comparative techno-economic analysis on CO2-to-methanol and CO_2-EOR. *Appl Energy* **388**, 125698 (2025).
5. Lemmon, J. P. Energy: Reimagine fuel cells. *Nature 2015 525:7570* **525**, 447–449 (2015).
6. Klemeš, J. J. *et al.* Sustainable energy integration within the circular economy. *Renewable and Sustainable Energy Reviews* **177**, 113143 (2023).
7. Hydrogen Storage | Department of Energy. https://www.energy.gov/eere/fuelcells/hydrogen-storage.
8. Mao, S. S. & Shen, S. Hydrogen production: Catalysing artificial photosynthesis. *Nat Photonics* **7**, 944–946 (2013).
9. Lin, H., Luo, S., Zhang, H. & Ye, J. Toward solar-driven carbon recycling. *Joule* **6**, 294–314 (2022).
10. Sacco, A. *et al.* An Integrated Device for the Solar-Driven Electrochemical Conversion of CO2to CO. *ACS Sustain Chem Eng* **8**, 7563–7568 (2020).
11. Rahaman, M. *et al.* Solar-driven liquid multi-carbon fuel production using a standalone perovskite–BiVO4 artificial leaf. *Nature Energy 2023 8:6* **8**, 629–638 (2023).
12. Chen, X. *et al.* Promoting water dissociation for efficient solar driven CO2 electroreduction via improving hydroxyl adsorption. *Nature Communications 2023 14:1* **14**, 1–12 (2023).
13. Rashid, N., Yang, S. & Abdi Jalebi, M. Socio-Economic Impact and Regulatory Measurements for Next-Generation Electrochemical CO_2 Conversion System. *Nanoscale and Advanced Materials* **2**, 1–9 (2025).
14. Lamb, W. F. & Rao, N. D. Human development in a climate-constrained world: What the past says about the future. *Global Environmental Change* **33**, 14–22 (2015).
15. Staffell, I. *et al.* The role of hydrogen and fuel cells in the global energy system. *Energy Environ Sci* **12**, 463–491 (2019).
16. Rashid, N., Bhat, M. A. & Ingole, P. P. Unravelling the chemistry of catalyst surfaces and solvents towards C–C bond formation through activation and electrochemical conversion of CO 2 into hydrocarbons over micro-structured dendritic copper. *Sustain Energy Fuels* **6**, 128–142 (2021).
17. Rashid, N., Dar, F., Bhat, M. & Ingole, P. Tailoring Motif and Channel Terminating Groups of Conventional Copper MOFs for Their Enhanced Activity, Selectivity, and Stability toward the Electroreduction of CO_2 to Hydrocarbons. *ACS Appl Energy Mater* **6**, 1378–1388.
18. Yang, F. *et al.* Highly efficient electroconversion of carbon dioxide into hydrocarbons by cathodized copper-organic frameworks. *Chem Sci* **10**, 7975–7981 (2019).
19. Weng, Z. *et al.* Active sites of copper-complex catalytic materials for electrochemical carbon dioxide reduction. *Nature Communications 2018 9:1* **9**, 1–9 (2018).
20. Karaiskakis, A. N., Golru, S. S. & Biinger, E. J. Effect of Electroe Geometry on Selectivity an Activity in CO2 Electroreuction. *Ind Eng Chem Res* **58**, 22506–22515 (2019).
21. Astakhov, O., Cibaka, T., Wieprecht, L., Rau, U. & Merdzhanova, T. Unfolding Electrolyzer Characteristics to Reveal Solar-to-Chemical Efficiency Potential: Rapid Analysis Method Bridging Electrochemistry and Photovoltaics. *ChemSusChem* **18**, e202402027 (2024).
22. Angeles-Olvera, Z. *et al.* Nickel-Based Electrocatalysts for Water Electrolysis. *Energies*

2022, Vol. 15, Page 1609 **15**, 1609 (2022).

23. Irshad, A. & Munichandraiah, N. Electrodeposited Nickel-Cobalt-Sulfide Catalyst for the Hydrogen Evolution Reaction. *ACS Appl Mater Interfaces* **9**, 19746–19755 (2017).
24. Pašti, I. A. *et al.* Atomically Thin Metal Films on Foreign Substrates: From Lattice Mismatch to Electrocatalytic Activity. *ACS Catal* **9**, 3467–3481 (2019).
25. Heikkinen, M., Ghiyasi, R. & Karppinen, M. Layer-Engineered Functional Multilayer Thin-Film Structures and Interfaces through Atomic and Molecular Layer Deposition. *Adv Mater Interfaces* **12**, 2400262 (2025).
26. Lim, C. Y. J., Handoko, A. D. & Seh, Z. W. A realistic take on MXenes for electrochemical reduction of carbon dioxide. *Diam Relat Mater* **130**, 109461 (2022).
27. Meng, L., Tayyebi, E., Exner, K. S., Viñes, F. & Illas, F. MXenes as Electrocatalysts for the CO2 Reduction Reaction: Recent Advances and Future Challenges. *ChemElectroChem* **11**, e202300598 (2024).
28. Handoko, A. D. *et al.* Two-Dimensional Titanium and Molybdenum Carbide MXenes as Electrocatalysts for CO2 Reduction. *iScience* **23**, 101181 (2020).
29. Li, N. *et al.* Understanding of Electrochemical Mechanisms for CO2 Capture and Conversion into Hydrocarbon Fuels in Transition-Metal Carbides (MXenes). *ACS Nano* **11**, 10825–10833 (2017).
30. Govindan, B. *et al.* Synergistic Bimetallic Sites in 2D-on-2D Heterostructures for Enhanced C-N Coupling in Sustainable Urea Synthesis. *ACS Sustain Chem Eng* **12**, 8174–8187 (2024).
31. Wang, R. *et al.* Element-Doped Mxenes: Mechanism, Synthesis, and Applications. *Small* **18**, 2201740 (2022).
32. Cao, S. *et al.* MXene-based single atom catalysts for efficient CO2RR towards CO: A novel strategy for high-throughput catalyst design and screening. *Chemical Engineering Journal* **461**, 141936 (2023).
33. Kumar Sharma, P., Rashid, N. & Abdi Jalebi, M. Safe-by-Design Approach for Next-Generation Electrochemical CO_2 Conversion Prototype with Risk Assessment and Safety Considerations. *Nanoscale and Advanced Materials* **2**, 74–83 (2025).
34. Fang, B. *et al.* Large-scale synthesis of TiO2microspheres with hierarchical nanostructure for highly efficient photodriven reduction of CO2to CH4. *ACS Appl Mater Interfaces* **6**, 15488–15498 (2014).
35. Somoza-Tornos, A., Guerra, O. J., Crow, A. M., Smith, W. A. & Hodge, B. M. Process modeling, techno-economic assessment, and life cycle assessment of the electrochemical reduction of CO2: a review. *iScience* vol. 24 Preprint at https://doi.org/10.1016/j.isci.2021.102813 (2021).
36. Wyndorps, J., Ostovari, H. & von der Assen, N. Is electrochemical CO2reduction the future technology for power-to-chemicals? An environmental comparison with H2-based pathways. *Sustain Energy Fuels* **5**, 5748–5761 (2021).
37. Zlatar, M. *et al.* Standardizing OER Electrocatalyst Benchmarking in Aqueous Electrolytes: Comprehensive Guidelines for Accelerated Stress Tests and Backing Electrodes. *ACS Catal* 15375–15392 (2023).
38. Marini, S. *et al.* Advanced alkaline water electrolysis. *Electrochim Acta* **82**, 384–391 (2012).
39. Miao, M., Duan, H., Luo, J. & Wang, X. Recent progress and prospect of electrodeposition-type catalysts in carbon dioxide reduction utilizations. *Mater Adv* **3**, 6968–6987 (2022).

40. Zangari, G. Fundamentals of Electrodeposition. *Encyclopedia of Interfacial Chemistry: Surface Science and Electrochemistry* 141–160 (2018).
41. Guruprasad, N., van der Schaaf, J. & de Groot, M. T. Unraveling the impact of reverse currents on electrode stability in anion exchange membrane water electrolysis. *J Power Sources* **613**, 234877 (2024).
42. Rashid, N., Ingole, P. P. & Delhi, N. Electrochemical Reduction of CO 2 on Ionic Liquid Stabilized Reverse Pulse Electrodeposited Copper Oxides. **2**, 1–9.
43. Reverse Pulse Electrodeposition of Copper Octahedrons: CO_2RR on These Edges. Indian Institute of Technology Delhi.
44. Voncken, J. H. L. & Verkroost, T. W. Powder diffraction of cubic α-brass. *Powder Diffr* **12**, 228–229 (1997).
45. Salehi, M., Saidi, A., Ahmadian, M. & Raeissi, K. Characterization of Nanocrystalline Nickel-Cobalt Alloys Synthesized by Direct and Pulse Electrodeposition. *IJMPB* **28**, 1450043 (2014).
46. Walsh, F. C. & Herron, M. E. Electrocrystallization and electrochemical control of crystal growth: fundamental considerations and electrodeposition of metals. *J Phys D Appl Phys* **24**, 217 (1991).
47. Shi, Y. *et al.* Atomic-Level Metal Electrodeposition: Synthetic Strategies, Applications, and Catalytic Mechanism in Electrochemical Energy Conversion. *Small Struct* **3**, 2100185 (2022).
48. Kaneco, S., Iiba, K., Hiei, N. & Ohta, K. Electrochemical reduction of carbon dioxide to ethylene with high Faradaic efficiency at a Cu electrode in CsOH / methanol. **44**, 4701–4706 (1999).
49. Lv, W., Zhang, R., Gao, P. & Lei, L. Studies on the faradaic efficiency for electrochemical reduction of carbon dioxide to formate on tin electrode. *J Power Sources* **253**, 276–281 (2014).

Images of the paper as a separate file.

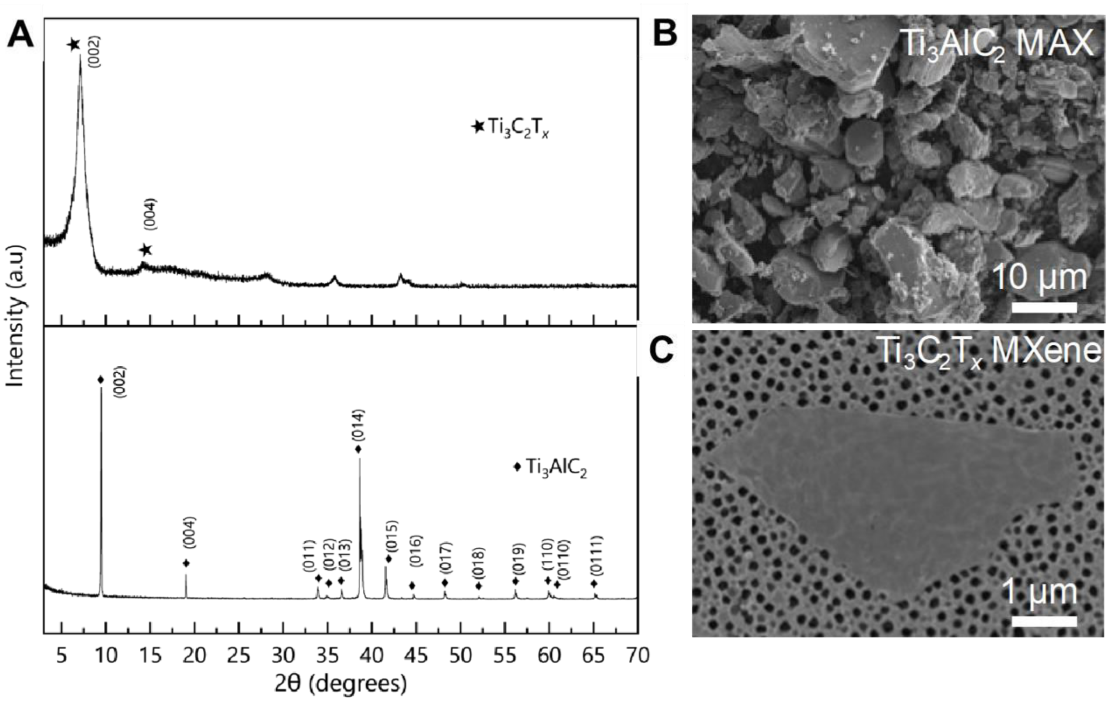

Figure 1: (A) XRD pattern showing characteristic peaks for $Ti_3C_2T_x$ (indicated by stars) and Ti_3AlC_2 MAX phase (indicated by diamonds); (B) SEM image of Ti_3AlC_2 MAX phase; (C) SEM image of delaminated $Ti_3C_2T_x$ MXene.

C

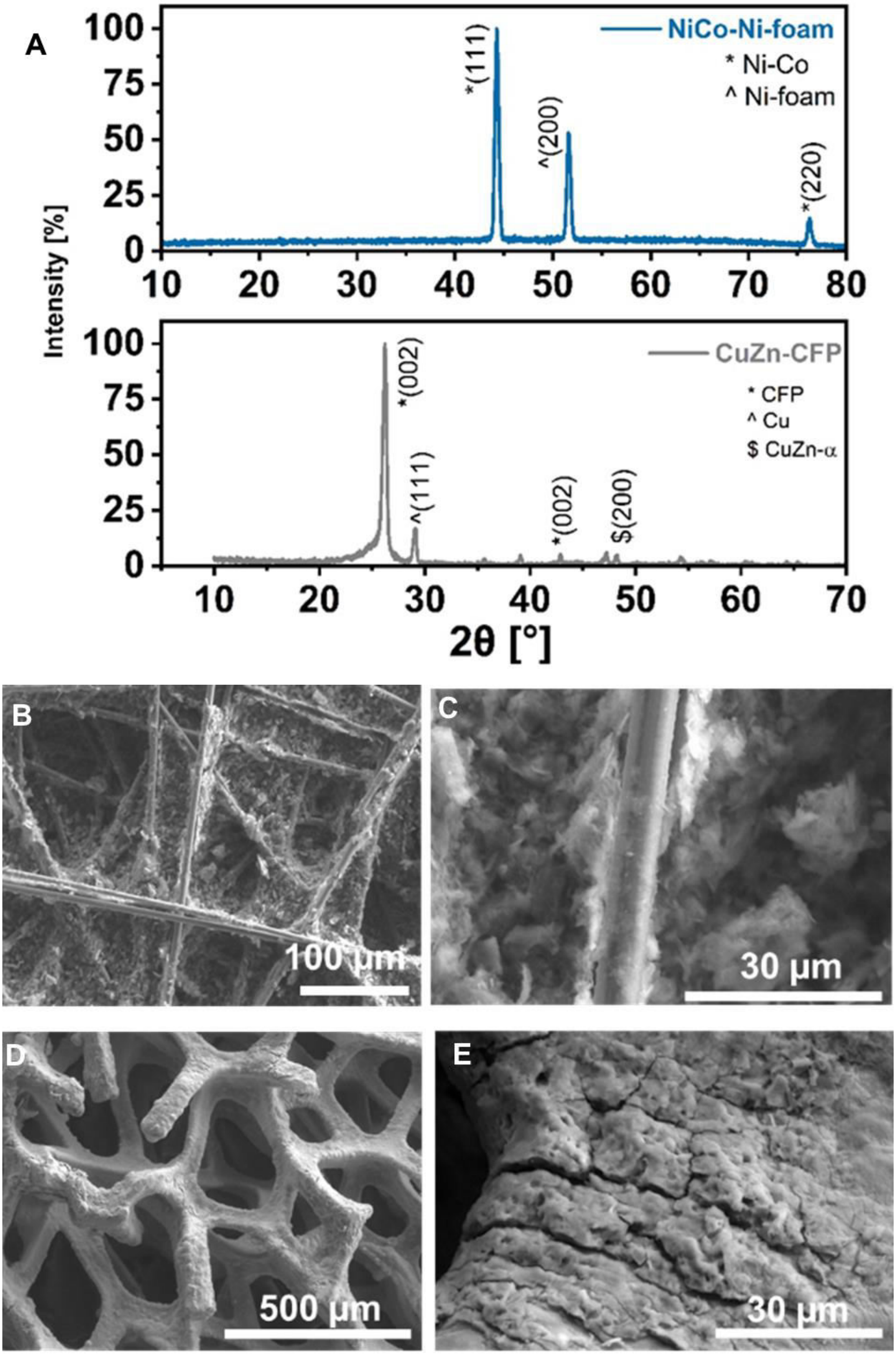

Figure 2: XRD (A) and SEM images of the fabricated bi-metallic electrocatalyst films, CuZn@$Ti_3C_2T_x$ MXene@CFP cathode for CO_2 reduction (B and C), and NiCo@$Ti_3C_2T_x$

MXene@Ni-F anode for water electrolysis (D and E).

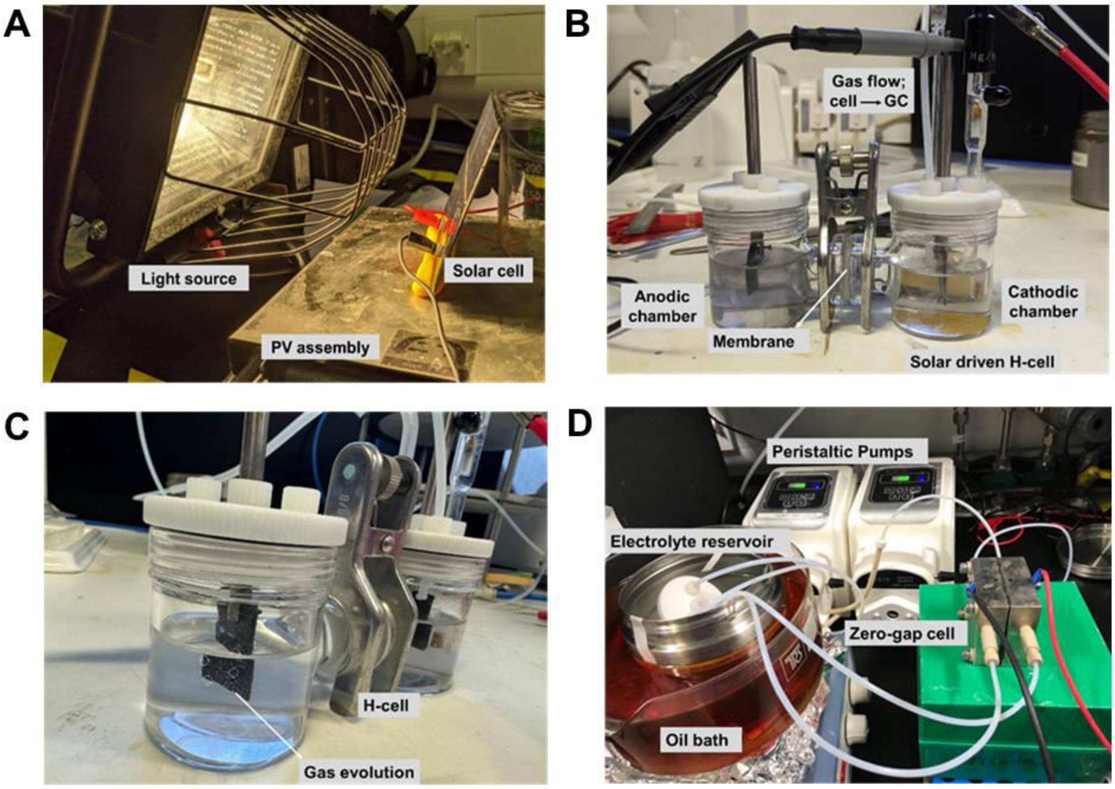

Figure 3: (A) PV assembly used to drive the electrochemical reduction of CO_2 and water at zero applied current, (B) H-cell used to reduce CO_2 and electrolyze water with a membrane to stop product oxidation, (C) gas bubbles observed on cathode when connected to the terminals of PV cell showing the reaction taking place, and (D) zero-gap cell assembly used to perform water electrolysis at industrial parameters (30% KOH, 1 A/cm^2, 60 ^{o}C).

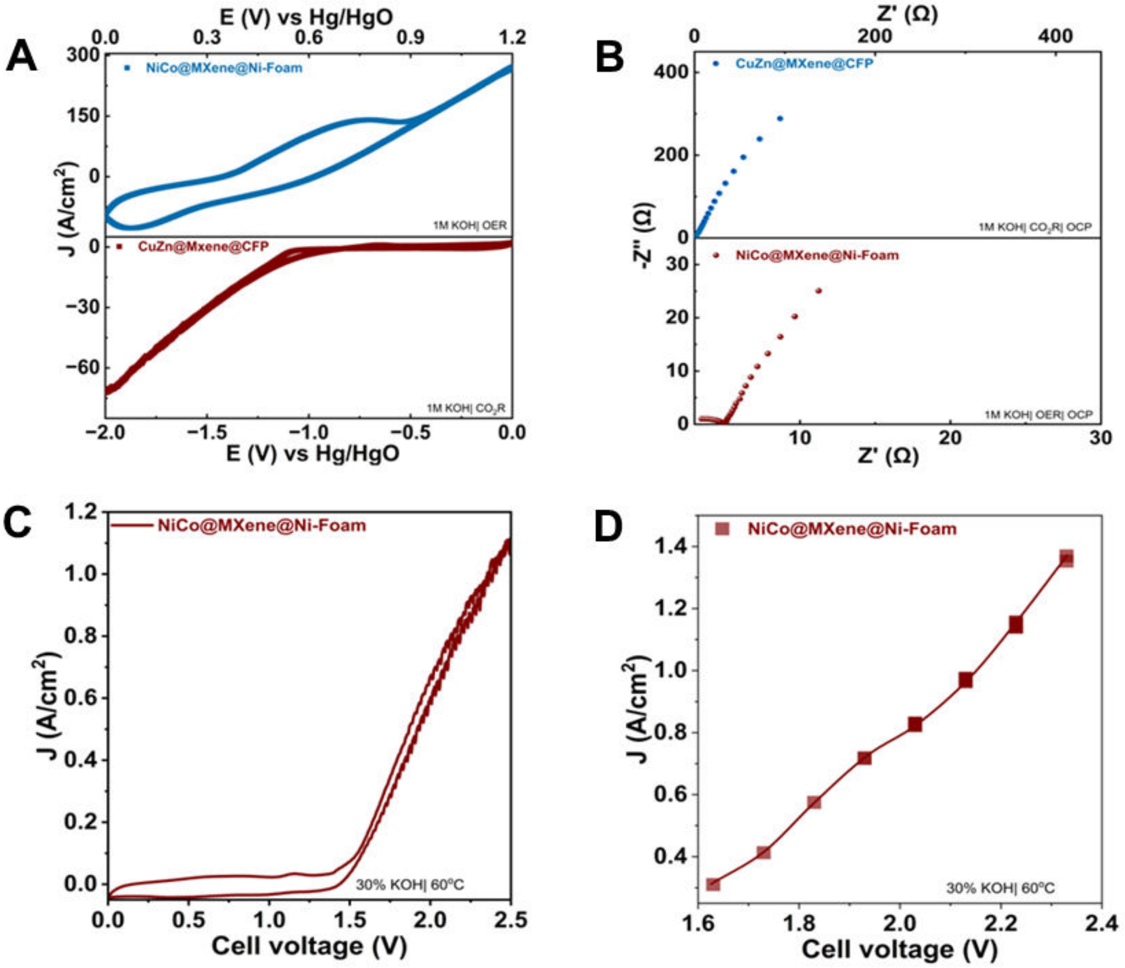

Figure 4: (A) CV obtained in 1 M KOH in a H-cell for CO_2 reduction (CO_2R) (red trace), and OER (blue trace) using H-cell assembly, (B) EIS at open circuit potential for anode and cathode in CO_2R and water electrolysis, (C) CV and (D) chrono amperograms observed at different applied cell potentials (1.6 V to 2.6 V on NiCo@MXene@Ni-Foam anode in 30% KOH, 60 ^{o}C, and electrolyte flow rate of 50 mL/min in a zero-gap cell (mimicking commercial AEM-WE).